ACS APPLIED MATERIALS & INTERFACES

www.acsami.org

Research Article

Coking- and Sintering-Resistant Ni Nanocatalysts Confined by Active BN Edges for Methane Dry Reforming

Xiaoyu Zhang,[†] Jiang Deng,[†] Tianwei Lan, Yongjie Shen, Wenqiang Qu, Qingdong Zhong, and Dengsong Zhang*

Cite This: *ACS Appl. Mater. Interfaces* 2022, 14, 25439−25447

Read Online

ACCESS | Metrics & More | Article Recommendations | Supporting Information

ABSTRACT: Methane dry reforming (MDR) has attracted significant attention for effectively consuming greenhouse gases and producing valuable syngas. The development of coking- and sintering-resistant catalysts is still a challenge. Herein, highly active Ni nanocatalysts confined by the active edges of boron nitride have been originally developed, and the coking- and sintering-resistant MDR mechanism has also been unraveled. The active edges of boron nitride consisted of boundary BO_x species interact with Ni nanoparticles (NPs), which can contribute to the activation of both CH_4 and CO_2. The etching of BN is restrained under the buffer of boundary BO_x species. Operando spectra reveal that the formation and conversion of active bicarbonate species is accelerated by the boundary BO_x species. The complete decomposition of CH_4 is suppressed, and thus the coke formation is restricted. The functional groups of active BN edges are confirmed to stabilize the Ni NPs and facilitate the MDR reaction. This work provides a novel approach for the development of coking- and sintering-resistant catalysts for MDR.

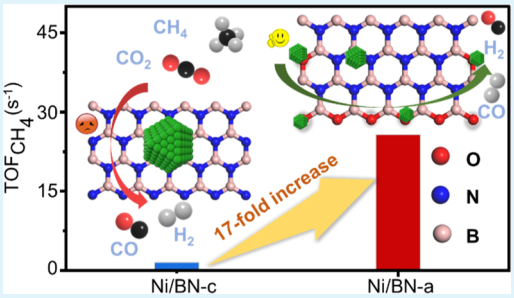

KEYWORDS: *methane dry reforming, boron nitride, Ni-based catalysts, coking resistance, sintering resistance*

1. INTRODUCTION

Methane dry reforming (MDR) is of particular interest from the perspective of economic development and has long been considered as a valuable method for the conversion of CH_4 and CO_2 into syngas. The stoichiometry syngas produced in MDR is suitable for preparing high value-added chemicals via Fischer−Tropsch synthesis, which is also crucial for mitigating greenhouse gas emissions.[1−3] Considering the low cost and comparable activity with noble metals, Ni-based catalysts have become one of the most promising choices for MDR. However, coking and sintering of active metal causes the serious deactivation of Ni-based catalysts during the MDR process.[4−6] Traditional strategies to solve these problems are controlling the Ni particle size via well-confined structured catalysts,[7−9] utilizing basic supports to enrich the surface oxygen vacancies,[10−13] and adding the secondary metals to increase the dispersion of Ni particles.[14−17] Most of the strategies mentioned in the literature utilize metal oxides as the support of catalysts, which can promote the catalytic activity significantly. Nevertheless, the coking issue is still a formidable one to eliminate.

Recently, hexagonal boron nitride (h-BN) has attracted much attention due to its excellent thermal conductivity and chemical stability.[18,19] The unique surface chemical and electronic properties of h-BN make it widely applicable in catalysis, such as photocatalysis, oxidative dehydrogenation, and CO oxidation,[20−25] and MDR, where the h-BN displays excellent coke resistance.[26−29] However, the surface inertia of pristine h-BN restrains the dispersion of the supported active metal, leading to weak metal−support interaction.[30,31] Therefore, the essentiality of constructing defects on the h-BN surface has been recognized.[32] In particular, Lin et al.[33] clarifies that Pt ions can be stabilized at the terminal oxygen species at the edge of h-BN. Meanwhile, as proposed by Grant et al.,[21] the terminal oxygen at the boundary of h-BN can be used as the catalytic active site in the selective oxidative dehydrogenation of propane. Moreover, our previous work also proves that the BN exposed more B terminal can stabilize Ni particles and illustrates that B−OH is beneficial for the catalytic activity during the MDR process.[34,35] However, the underlying mechanism of B−O for the improvement of the MDR reaction is still unclear. Additionally, Dong et al.[36] demonstrate that the strong metal−support interaction is triggered by the BOx species derived from h-BN during the MDR reaction. Theoretical simulation results demonstrate that B−O and B−OH sites in the BO_x and Ni sites promote the MDR

Received: March 7, 2022
Accepted: May 13, 2022
Published: May 23, 2022

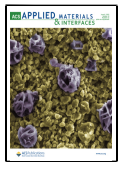

Downloaded via TSINGHUA UNIV on October 6, 2023 at 06:51:16 (UTC).
See https://pubs.acs.org/sharingguidelines for options on how to legitimately share published articles.

© 2022 American Chemical Society

https://doi.org/10.1021/acsami.2c04149
ACS Appl. Mater. Interfaces 2022, 14, 25439−25447

performance synergistically. However, the etch of h-BN destroys the support to a certain extent.

In this work, coking- and sintering-resistant highly active Ni nanocatalysts confined by active edges of boron nitride have been originally developed. The boundary BO_x species are proved as the active edges over BN to stabilize Ni particles, arising strong sintering resistance of active Ni. The etching of BN is inhibited under the buffer of boundary BO_x species. The mutipulse coupling online mass spectrometry (MS) experiments reveal that the activation of CH_4 and CO_2 is enhanced by the synergistic effects of boundary BO_x species and Ni. The operando diffuse reflectance infrared Fourier transform spectroscopy (DRIFTS) experiments confirm that the boundary BO_x species are extremely involved in the formation and conversion of bicarbonate (*HCO_3) species. Meanwhile, it is found that CH_4 can accelerate the evolution of intermediates, raising the reaction rate. The full decomposition of CH_4 is suppressed, suggesting that the coke formation is restricted based on the operando Raman spectra results. This work provides a novel approach for the development of coking- and sintering-resistant Ni nanocatalysts for MDR.

2. EXPERIMENTAL SECTION

Boron nitride with active edges (BN-a) was prepared by a pyrolysis method.[37,38] As a comparison, the boundary BO_x species over BN-a were removed and labeled BN-w. The detailed preparation of BN-a and BN-w is shown in the Supporting Information. Ni/BN-a catalysts were prepared by an impregnation method. A certain amount of BN-a powder was added into the Ni $(NO_3)_2{\cdot}6H_2O$ aqueous solution with stirring for 6 h, and then dried via rotary evaporation at 60 °C. The obtained samples were calcined at 550 °C for 6 h in a muffle furnace, and the resultant powder was named NiO/BN-a. The calcined samples were then reduced in H2 at 750 °C for 1 h in 10% H_2/N_2 (30 $mL{\cdot}min^{-1}$) and the resultant catalyst was named Ni/BN-a. The preparation method of Ni/BN-w and Ni/BN-c (commercial BN) was the same as for Ni/BN-a. The content of Ni was controlled to 1 wt %. The characterizations of the obtained catalysts can be found in the Supporting Information.

3. RESULTS AND DISCUSSION

3.1. Characteristic of Catalysts. X-ray powder diffraction (XRD) was performed to investigate the crystalline structure of supports and catalysts. The diffraction peaks of BN-a and BN-w (Figure S1) are indexed as the (002), (100), (004), and (110) planes (PDF#34-0421) of h-BN as uncovered by XRD patterns. High-resolution transmission electron microscopy (HRTEM) images (Figure S2) exhibit the (002) and (100) planes of BN-a. Compared with the large flakes of BN-c, the synthesized BN-a shows nanosize sheets (Figures S3 and S4). The nanosheets of BN-a are then extensively stacked, forming bulk BN, which is beneficial for improving the sintering resistance of the catalysts (Figure S3a,b). The crystal structures of BN-a and BN-c remain well after loading Ni, as shown in Figure 1a. Meanwhile, no diffraction peak belonging to Ni (111) at 44.5° is observed in the Ni/BN-a catalysts, which can be assigned to the well dispersion of Ni over Ni/BN-a catalysts. On the contrary, an obvious Ni (111) diffraction peak is present in the Ni/BN-w and Ni/BN-c patterns. The abovementioned results suggest that, compared with BN-w and BN-c, Ni can be dispersed well on BN-a. The TEM image displays the morphology of stacked nanosheets of BN-a (Figures S3−S5). It can also be seen that Nia is uniformly dispersed on BN-a with an average Ni nanoparticle (NP) size of 4.5 nm (Figure S5). Figure 1b also displays the TEM image

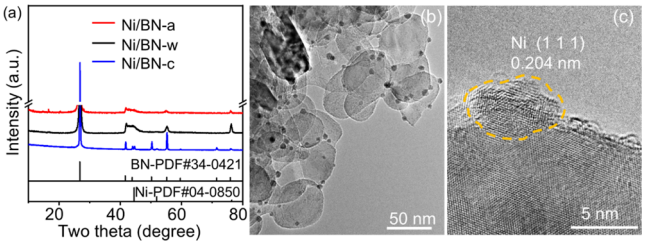

Figure 1. (a) XRD patterns of the reduced catalysts. (b) TEM and (c) HRTEM images of Ni/BN-a catalysts.

of Ni/BN-a catalysts, verifying that most of the Ni NPs are located at the edge of BN-a. HRTEM in Figure 1c provides the Ni particle with a lattice fringe spacing of 0.204 nm, corresponding to the (111) surface of Ni. In addition, Ni particles present irregular shapes, testifying that the BN-a with abundant active edges influences the crystalline process of Ni, resulting in more specific active sites (edge and step sites) on the Ni NPs.[39]

Generally, h-BN has high chemical stability, which is inert for loading metal particles. The anomalous well dispersion of Ni over BN-a suggests the heightened interaction of the Ni NPs and support. The BN supports were explored by X-ray photoelectron spectroscopy (XPS) combined with Fourier transform infrared (FTIR) spectra to explore the surface properties. The peak at 191.4 eV is assigned to B−O in the B 1s spectra of BN-a with a content of 10.9% (Figure 2a),[40]

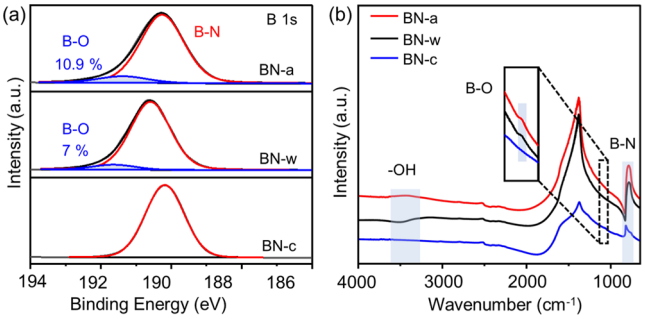

Figure 2. (a) B 1s XPS spectra and (b) FTIR spectra of BN-a, BN-w, and BN-c. The inset in (b) is the enlarged labeled section.

suggesting the abundant existence of boundary boron oxide (BO_x) species. As proposed by Liu et al., the supported metal can be anchored to the terminal oxygen species at the edge of h-BN. Meanwhile, the small size of BN-a (Figure S5) provides more boundary oxygen species within the boundary region for the deposition of metal.[20] The decreased B−O ratio after loading Ni proves that Ni NPs are anchored in the boundary region of BN-a (Figure S6). Hence, the abundant boundary BO_x species as the active edges of BN-a enable well dispersion of Ni NPs. It is worth noting that there are no B−O species in the B 1s spectra of BN-c, suggesting the perfect crystallinity of BN-c, which is inert for the dispersion of Ni, resulting in the large size and poor dispersion of Ni NPs as shown in the TEM image of Ni/BN-c (Figure S7b). The large size and poor dispersion of Ni NPs on BN-c is also affected by the small surface area (Table 1). The BO_x species on the boundary region of BN-a were removed by calcined in air at 800 °C and washed with water to further prove the importance of boundary oxygen species for the deposition of Ni NPs, which was labeled BN-w. The B 1s spectra of BN-w display

https://doi.org/10.1021/acsami.2c04149
ACS Appl. Mater. Interfaces 2022, 14, 25439−25447

Table 1. Physicochemical Properties of the Reduced Catalysts

catalysts	ICP–AES[a] Ni (wt %)	N_2 physisorption[b] S_{BET} [m^2/g]	metal[c] dispersion (%)	H_2 consumption[d] [$mmol_{H2}/g_{cat}$]	particle size of fresh catalysts [nm]
Ni/BN-c	0.9	3	4.6	0.25	32.5[e]
Ni/BN-a	1.1	76.9	8.3	0.29	4.5[f]
Ni/BN-w	1.1	62.7	6.4	0.26	7.6[f]

[a]Nickel loading was determined by elemental analysis. [b]The specific surface area was calculated using Brunauer–Emmett–Teller models. [c]Measured by H_2 pulse chemisorption. [d]H_2 consumption was determined by the H_2-TPR experiment. [e]Calculated by the Scherrer equation. [f]Ni particle size determined by TEM images.

that the percentage of B–O decreases from 10.9% (BN-a) to 7%. The larger average size of Ni NPs in the TEM image of the Ni/BN-w catalysts (Figure S7a) signifies that the decreased boundary BO_x species probably influence the dispersion and particle size of Ni over BN-w (Table 1). The B–O species are also corroborated by FTIR spectra (Figure 2b). A broad feature at 3450 cm^{-1} and a sharp signal at 1235 cm^{-1} are shown in the FTIR spectra of BN-a and BN-w, which can be attributed to the OH– and B–O stretching vibrations, respectively.[21,41,42] The peaks of OH– and B–O did not appear in BN-c spectra, in accordance with B 1s XPS results.

The active edges over BN-a were expected to form a strong interaction with Ni NPs. Hence, the chemical properties of Ni/BN-a, Ni/BN-w, and Ni/BN-c were explored by hydrogen temperature-programed reduction (H_2-TPR) (Figure 3a) and

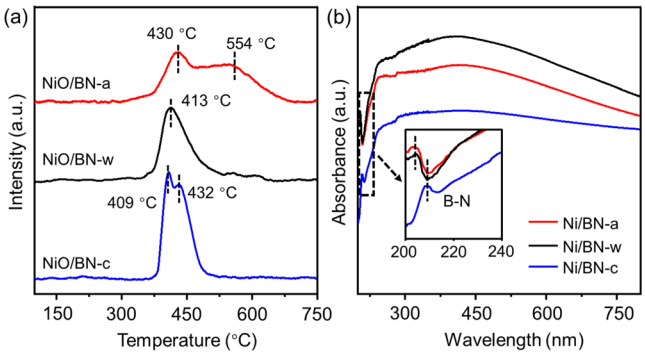

Figure 3. (a) TPR profiles of NiO/BN-a, NiO/BN-w, and NiO/BN-c. (b) UV–vis spectra of Ni/BN-a, Ni/BN-w, and Ni/BN-c catalysts. The inset in (b) is the enlarged labeled section.

ultraviolet–visible (UV–vis) diffuse reflectance spectra (Figure 3b). All the catalysts show the reduction peak between 400 and 440 °C which can be attributed to the Ni NPs loaded on the BN surface. The peak at 554 °C shown in the TPR profile of NiO/BN-a is ascribed to the reduction of NiO_x species located at the active edges of BN-a. The higher reduction temperature implies that the NiO_x–boundary interaction over BN-a is stronger than the NiO_x–surface interaction.[20] UV–vis spectra (Figure 3b) were employed to further confirm the interaction between Ni and BN-a by monitoring the local electron state of the catalysts. The peak at 200–210 nm belongs to $\sigma \rightarrow \sigma^*$ in B–N.[37] The spectra of Ni/BN-a and Ni/BN-w express an obvious blue shift compared with Ni/BN-c, indicating that the electrons are delivered from B to Ni. Therefore, it can be concluded that there is a strong interaction between Ni and the active edges over BN-a.

3.2. Catalytic Performance. The activity of as-prepared catalysts was subjected to the MDR reaction at 700 °C with 80 mg of catalysts loaded under a constant stream of CH_4/CO_2 (25/25 $mL \cdot min^{-1}$). As shown in Figure 4a, the Ni/BN-a catalysts display the highest initial activity among the BN-

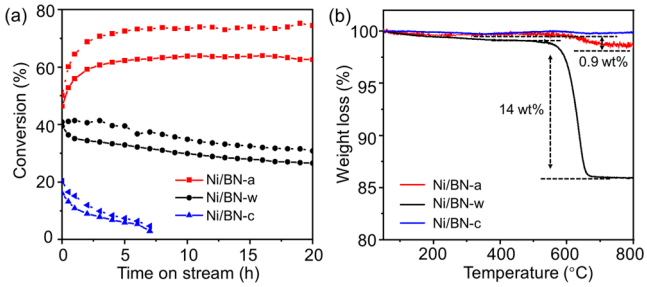

Figure 4. (a) Plots of CH_4 (solid line) and CO_2 (dash line) conversion vs time on stream over the reduced catalysts. (b) TG profiles of the used catalysts after the 20 h MDR reaction. The performance was carried out at 700 °C with gas hourly space velocity (GHSV) of 37500 $mL \cdot g_{cat}^{-1} \cdot h^{-1}$.

supported Ni nanocatalysts with CH_4 and CO_2 conversion of 46.4 and 50.2%, respectively. The low initial activities of the Ni/BN-w and Ni/BN-c catalysts probably derive from the less boundary BO_x species over the BN-w and BN-c. During the long-term MDR reaction, the conversion of CH_4 and CO_2 gradually increases to 63.9 and 73.9%, respectively, and keeps constant during the 20 h operation. The increased activity of Ni/BN-a catalysts can be attributed to the re-dispersion of Ni particles during the MDR reaction. It is confirmed by the increased metal dispersion (10.4 versus 8.4%) after 2 h MDR reaction. The dispersion of Ni particles over the spent Ni/BN-a catalysts is not affected by the carbon deposition, as evidenced by the negligible weight loss of the spent Ni/BN-a catalysts after 2 h of the MDR reaction (Figure S8). The Ni/BN-a catalysts exhibit excellent stability, even extending the MDR process to 40 h (Figure S9a). Meanwhile, the Ni/BN-w and Ni/BN-a catalysts suffer rapid deactivation during the 20 h MDR reaction (Figure 4a), which may be caused by the carbon deposition or the agglomeration of Ni particles. The deposited carbon over the catalysts after a 20 h stability test at 700 °C was measured by thermogravimetric (TG) analysis (Figure 4b). The Ni/BN-a catalysts display excellent coking resistance with only 0.9 wt % of the weight loss. By contrast, a weight loss of 14 wt % is observed over the spent Ni/BN-w, which results in the deactivation of Ni/BN-w catalysts. A negligible weight loss is observed in the spent Ni/BN-c due to the low activity of this catalyst. The grain size of the fresh and spent Ni/BN-c catalysts was calculated based on the Scherrer equation according to XRD patterns (Figures 1a and S10). The grain size of Ni over the spent Ni/BN-c catalyst is 46.3 nm, which increases by 13.8 nm compared to the fresh catalysts (32.5 nm, Table 1). Therefore, the serious sintering of Ni particles causes the rapid deactivation of the Ni/BN-c catalysts. The weight

https://doi.org/10.1021/acsami.2c04149
ACS Appl. Mater. Interfaces 2022, 14, 25439–25447

loss of Ni/BN-a catalysts after extending the test time to 40 h (Figure S9b) is 1.57%, which is higher than that of the catalysts after 20 h MDR reaction (0.9%). However, compared with the Ni/BN-w catalysts, the Ni/BN-a catalysts with abundant active edges (boundary BO_x) still exhibit excellent coke resistance. The conversion of CH_4 and CO_2 over different catalysts is also normalized by the surface area (Figure S11). The conversion over Ni/BN-c is much higher than the other catalysts; however, the distinctly low surface area (3 m^2/g, Table 1) might overstate the conversion rates. Hence, the turnover frequency of CH_4 (TOF_{CH4}) was measured for the catalysts to evaluate their intrinsic activity. The TOF_{CH4} over Ni/BN-a, Ni/BN-w, and Ni/BN-c catalysts (Table S1) is 13.5, 5.5, and 0.77 s^{-1}, respectively, suggesting that the intrinsic activity is improved by developing Ni/BN-a catalysts. The ratio of H_2/CO was analyzed to explore the side reactions (Figure S12). For Ni/BN-a and Ni/BN-w catalysts, the H_2/CO ratio is similar but slightly lower than one, which is caused by the reverse water−gas shift (RWGS) reactions ($CO_2 + H_2 \rightarrow CO + H_2O$). By comparison, the H_2/CO ratio of Ni/BN-c is much lower than 1, which is due to the low conversion of CH_4 and serious RWGS, leading to inferior stability.[43]

The capacity of coking resistance was explored by operando Raman as shown in Figure 5. Generally, disordered carbon and

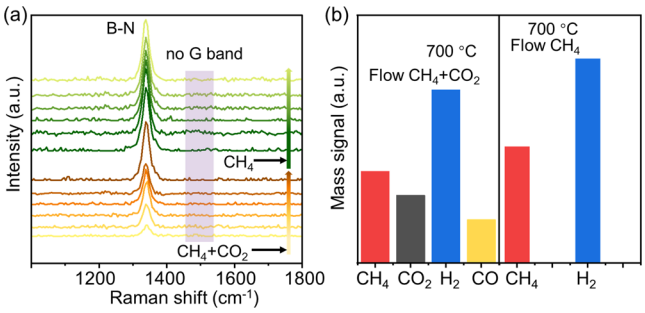

Figure 5. (a) Operando Raman spectra of Ni/BN-a catalysts at 700 °C by switching between different gases: flow $CH_4 + CO_2$ (10 + 10 mL·min^{-1}) for 30 min, and then flow CH_4 (10 mL·min^{-1}) for 30 min. (b) Mass signal of CH_4, CO_2, H_2, and CO during operando Raman experiment after flowing 30 min of $CH_4 + CO_2$ (10 + 10 mL·min^{-1}) and 30 min of CH_4 (10 mL·min^{-1}).

graphitic carbon appear at 1250−1350 and 1500−1700 cm^{-1}, respectively.[43,44] As shown in Figure 5a, only one band at 1365 cm^{-1} is observed, which can be assigned to the B−N band.[45,46] No related carbon bands appear during the flow of $CH_4 + CO_2$. In addition, online MS was carried out to monitor the products in the MDR process. In Figure 5b, after flowing CH_4 and CO_2 for 30 min, the signal intensity of reactants (CH_4 and CO_2) and the appearance of products (H_2 and CO) signals clarify that the MDR process occurs with no carbon formation (Figure 5a,b). To further verify the coking resistance, Ni/BN-a catalysts were exposed to CH_4 for 30 min. The H_2 formation suggests the occurrence of CH_4 cracking (Figure 5b). However, there is still no coke, as evidenced by the absence of G bands in the Raman spectra (Figure 5a). In the meantime, the large-scale two-dimensional Raman mapping proves that no coke was deposited on the catalysts (Figures S13 and S14). The results mentioned above indicate the excellent coking resistance of Ni/BN-a catalysts. Moreover, the Ni NPs size of Ni/BN-a after the 20 h MDR process is maintained well (Figure S15) with an average particle size of 5.1 nm, which only increases by 0.6 nm compared to the fresh catalysts. It indicates the abundant boundary O species over BN-a can stabilize Ni during the MDR process. Meanwhile, compared with the BN-supported Ni catalysts in the reported literature,[36] the etching of BN is suppressed during the MDR reaction, which is due to the buffer of the boundary BO_x species, avoiding the oxidation of nitrogen in BN-a during the reaction. As for Ni/BN-c, the agglomeration of Ni NPs happens accompanied by serious etching of BN-c (Figure S16), resulting in the deactivation. Above all, the Ni/BN-a catalysts display excellent initial activity, long-term stability, and coking and sintering resistance, even when compared with the reported literature (Table S1).

3.3. Surface Reaction Study. To identify the influence of rich boundary BO_x species on the catalysts on the reaction mechanism, temperature-programed desorption in CO_2 (CO_2-TPD) and CH_4-temperature-programed surface reaction (TPSR) were performed on the Ni/BN-a and Ni/BN-c catalysts. MS was carried out to monitor the desorption products in the process of CO_2-TPD (Figure 6). The CO_2

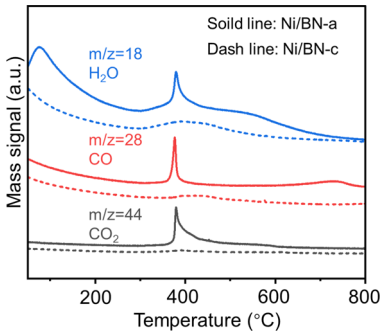

Figure 6. CO_2-TPD−MS profiles of Ni/BN-a and Ni/BN-c catalysts.

desorption peak over Ni/BN-a (solid line) is stronger than that of Ni/BN-c (dash line), as evidenced by the CO_2 signal, which indicates the improved adsorption quantity of CO_2 over Ni/BN-a catalysts. Meanwhile, an obvious CO signal appears in the mass profiles of Ni/BN-a, while the CO signal in the mass profiles of Ni/BN-c is negligible, suggesting that a chemisorption of CO_2 in Ni/BN-a catalysts can be activated. A strong signal of H_2O is observed over Ni/BN-a catalysts, which originates from the reaction between the O* species from CO_2 decomposition and the boundary B−OH species over BN-a. Figure S17 displays the CO_2-TPD−MS profiles of Ni/BN-w. The small amount of CO_2 desorption quantity and the weak CO signal suggest the poor ability of CO_2 adsorption and activation over Ni/BN-w catalysts. The results mentioned above reveal the strong adsorption and activation capability of CO_2 over Ni/BN-a catalysts.

CH_4-TPSR was performed to analyze the activation capacity of CH_4 of different catalysts, and the product composition was continuously monitored by online MS. Figure 7 shows the three-batch CH_4-TPSR experiments. The first CH_4-TPSR (Figure 7b) was conducted under CH_4 (30 mL·min^{-1}) from 50 to 800 °C after reducing the catalysts by H_2. The first CH_4-TPSR profiles of Ni/BN-a catalysts (Figure 7b, solid line) display that the CH_4 starts to decompose at 370 °C and then a small H_2 signal appears. Meanwhile, a strong signal of CO_2 at 370 °C is detected, suggesting the oxygen species over Ni/BN-a are involved into the reaction of CH_4 cracking. The appearance of H_2O at 370 °C suggests that the H* species

https://doi.org/10.1021/acsami.2c04149
ACS Appl. Mater. Interfaces 2022, 14, 25439−25447

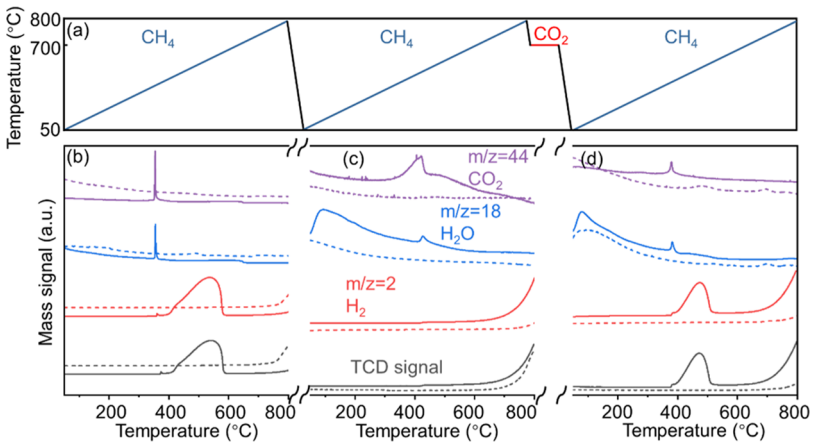

Figure 7. (a) Schematic illustration of CH_4-TPSR experiments. (b−d) CH_4-TPSR profiles of Ni/BN-a (solid line) and Ni/BN-c catalysts (dash line). (b) First CH_4-TPSR was conducted under CH_4 (30 mL·min^{-1}) from 50 to 800 °C after reducing the catalysts by H_2. (c) Second CH_4-TPSR was carried out after the first CH_4-TPSR using the same sample. (d) After the second CH_4-TPSR, the temperature was cooled down to 700 °C and then CO_2 was injected for 5 min. Subsequently, the temperature dropped to 50 °C and the third CH_4-TPSR was conducted.

from CH_4 cracking reacted with the boundary B−OH species or the absorbed oxygen on the surface of Ni/BN-a catalysts. This result reveals that a bit of NiO bound strongly with boundary BO_x species is reduced under the CH_4 and H_2 atmospheres. These metallic Ni species are then involved in dissociating CH_4, with the maximum conversion at 540 °C and the sole production of H_2 at 400−590 °C. The conversion of CH_4 disappears after 590 °C due to the deposition of C* species on the Ni^0 surface. The second batch of CH_4-TPSR was carried out to explore the capacity of CH_4 activation over the catalysts after the consumption of boundary oxygen species during the first batch. The second CH_4-TPSR is initialed after this system being cooled down to 50 °C. Specifically, a small amount of CO_2 and H_2O are detected accompanied by a weak H_2 signal at 420 °C (Figure 7c), which clarifies that the capacity of CH_4 cracking declines after the consumption of boundary BO_x species. The continuous release of H_2 after 610 °C suggests the decomposition of CH_4 happens extendedly. After the second batch of CH_4-TPSR, the temperature was cooled down to 700 °C and then CO_2 was injected for 5 min. Subsequently, the temperature dropped to 50 °C and the third batch of CH_4-TPSR was conducted (Figure 7d). The CO_2 signal is detected again, suggesting that the BO_x species are regenerated after being treated by CO_2. In the meantime, CH_4 begin to decompose at 370 °C with the maximum conversion at 475 °C (Figure 7d). The three CH_4-TPSR experiments were also carried out on Ni/BN-w catalysts. Also, the results show that the catalysts with fewer boundary BO_x species have poor capacity for CH_4 activation (Figure S18). The results mentioned above reveal that the Ni−O−B species over Ni/BN-a catalysts can enhance the decomposition of CH_4. By contrast, as shown in the first CH_4-TPSR profiles of Ni/BN-c (Figure 7b, dash line), CH_4 begins to be dissociated at 700 °C and consumed in large quantities at 750−800 °C. Simultaneously, almost no CO_2 and H_2O signals are detected due to the absence of boundary BO_x species, which is proved by XPS and FTIR (Figure 2). The same trend is also observed in the second and third CH_4-TPSR profiles (Figure 7c,d, dash line) of Ni/BN-c catalysts, which illustrates the limited capacity for CH_4 cracking of Ni/BN-c catalysts.

To explore the influence of each reactant, the mutipulse coupling online MS experiments were carried out (Figure 8).

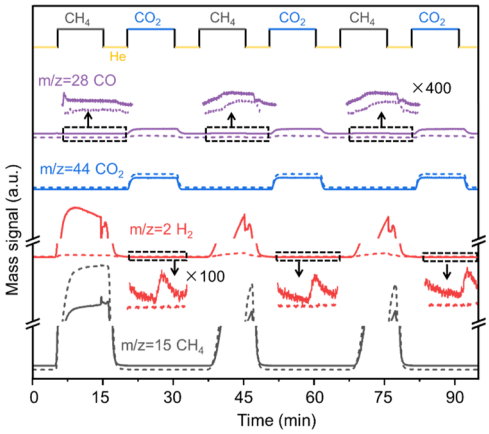

Figure 8. Mutipulse coupling online MS experiments were conducted at 540 °C (CH_4/CO_2 = 30/30 mL·min^{-1}) over Ni/BN-a (solid line) and Ni/BN-c (dash line) catalysts. CH_4 and CO_2 was injected for 10 min alternately with the He purged for 5 min in intermediate.

This experiment was conducted at 540 °C, where the maximum decomposition of CH_4 happens over the Ni/BN-a catalysts (Figure 7b). CH_4 was first introduced for 10 min. The H_2 signal is stronger over the Ni/BN-a catalysts than that of the Ni/BN-c catalysts, implying the enhanced CH_4 cracking capacity of the Ni/BN-a catalysts. Moreover, a weak CO signal is also detected over Ni/BN-a catalysts during the flow of CH_4. CO_2 was injected after cutting off CH_4 and purging with He for 5 min. The stronger CO signal over the Ni/BN-a proves the higher CO_2 activation ability over the Ni/BN-a catalyst. Meanwhile, a small H_2 signal is detected in the Ni/BN-a catalysts, which may be caused by the decomposition of surface deposited carbonate species derived from the reaction between CO_2 and boundary hydroxyl species. This result mentioned above suggests that the boundary BO_x species can involve the reaction. By contrast, no H_2 is produced in the Ni/BN-c catalysts during the same process due to the absence of boundary hydroxyl species. Afterward, CH_4 was introduced again for 10 min. The conversions of CH_4 over both Ni/BN-a and Ni/BN-c catalysts decrease compared with the first injection of CH_4. In the meantime, CO is detected on these two catalysts, which can be assigned to the side reaction

https://doi.org/10.1021/acsami.2c04149
ACS Appl. Mater. Interfaces 2022, 14, 25439−25447

between H_2 and the residual CO_2 (RWGS). The weak H_2 signal over Ni/BN-c implies the poor selectivity of H_2. The same experimental phenomenon is also observed in subsequent pulse experiments. The results mentioned above demonstrate that CH_4 and CO_2 are more easily activated over the Ni/BN-a catalysts and the boundary BO_x species on Ni/BN-a are involved in the reaction and beneficial for the production of H_2.

3.4. Mechanism Study. Operando DRIFTS (Figure 9) was carried out to analyze the intermediate species during the

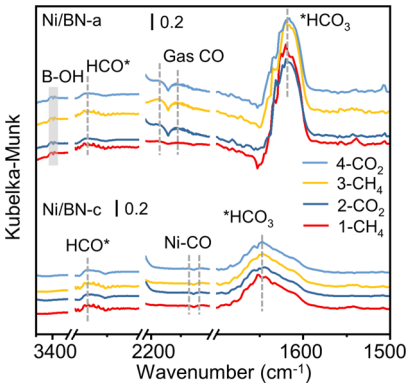

Figure 9. Operando DRIFTS of Ni/BN-a and Ni/BN-c catalysts conducted at 700 °C. CH_4 and CO_2 (10 and 10 mL·min^{-1}) was injected for 2 min alternately.

MDR process with online MS to monitor the desorption products (Figures S20 and S21). The different mechanisms are revealed in the Ni/BN-a and Ni/BN-c catalysts. The bands detected at 3365−3435 cm^{-1} can be assigned to B−OH species.[47,48] The double bands of gaseous CO appear at 2120 and 2170 cm^{-1}, while the bands at 2030 and 2070 cm^{-1} are assigned to the linearly adsorbed CO on Ni.[49−51] The formate (HCO*) and bicarbonate species (*HCO_3) appear at 2765 and 1620−1650 cm^{-1}, respectively.[52−54] During the alternate injection of CH_4 and CO_2 for four times, the HCO*, CO, and *HCO_3 species are detected over both the Ni/BN-a and Ni/BN-c catalysts. Nevertheless, the products (CO species) are linearly adsorbed on Ni over the Ni/BN-c catalysts, while they are the gas phase over the Ni/BN-a catalysts, which evidences the easy desorption of CO on the Ni/BN-a catalysts. The CO signal of Ni/BN-a catalysts (Figure S20) in the MS is stronger than that of Ni/BN-c catalysts (Figure S21). The above-mentioned results demonstrate the high CO selectivity of the Ni/BN-a catalysts. In addition, the B−OH species only appear on Ni/BN-a catalysts, indicating the abundant boundary oxygen species. Because the *HCO_3 species are derived from the reaction of CO_2* and OH* or the reaction of CH* and boundary oxygen species,[55] the boundary BO_x species benefit from producing this intermediate, which is proved by the higher relative intensity of *HCO_3 on the Ni/BN-a catalysts (Figure 9).

Figure 10 shows the intensity evolution of the intermediates during operando DRIFTS experiments, which reflects the catalytic behaviors of the Ni/BN-a and Ni/BN-c catalysts under different gases at 700 °C. During the first pulse of CH_4, *HCO_3 species (1620−1650 cm^{-1}) accumulate gradually, suggesting that CH* species are derived from the reaction between CH_4 and boundary oxygen species. In the meantime, both the accumulation rate and quantity of *HCO_3 on the Ni/

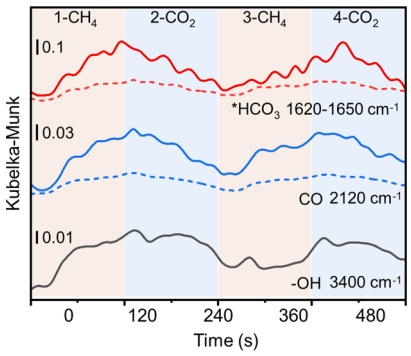

Figure 10. Intensity evolution of (a) *HCO_3, (b) CO, and (c) B−OH species from operando DRIFTS experiments over Ni/BN-a (solid line) and Ni/BN-c (dash line) catalysts during four periods at 700 °C. The pulse sequence was as follows: 1: CH_4 (10 mL·min^{-1}), 2: CO_2 (10 mL·min^{-1}), 3: CH_4 (10 mL·min^{-1}), and 4: CO_2 (10 mL·min^{-1}). Each pulse period was carried out for 2 min.

BN-a catalysts are significantly higher than those on the Ni/BN-c catalysts. In addition, the *HCO_3 can react with H* and then decompose into *HCO, CO, and −OH species. Hence, the intensity of CO (2120 cm^{-1}) and −OH (3400 cm^{-1}) species over the Ni/BN-a catalysts increases with the accumulation of *HCO_3. Simultaneously, the production rate and quantity of gaseous CO (2120 cm^{-1}) over Ni/BN-a are significantly higher than Ni−CO (2030 cm^{-1}) over the Ni/BN-c catalysts. During the second CO_2 pulse, the intensity of *HCO_3 species over both Ni/BN-a and Ni/BN-c decreases piecemeal, which can be ascribed to the reaction of *HCO_3 and O* (decomposed from CO_2) to form *CO_3 and −OH species. Due to the disappearance of H*, *HCO_3 species cannot be decomposed to CO, resulting in the decrease of CO species over both the Ni/BN-a and Ni/BN-c catalysts. Moreover, the decrease rates of *HCO_3 and gas CO species over the Ni/BN-a species are also higher than the Ni/BN-c catalysts. The rapid decrease of gas CO in DRIFTS suggests the strong desorption capacity of CO over the Ni/BN-a catalysts, resulting in the higher CO signal after flowing CO_2 as shown in MS (Figure S20). Generally, the O* or CO* decomposed from CO_2 can react with the surface hydroxyl, forming formate species, leading to the decline of −OH species. However, the amount of −OH species over the Ni/BN-a catalysts keep constant during the flowing of CO_2, further indicating that *HCO_3 species react with O* (decomposed from CO_2) to produce *CO_3 and −OH species. When the CH_4 was injected again, the intensity of all the intermediates increased gradually, which indicates that CH_4 might enhance the formation and the decomposition of the intermediates derived from CO_2, leading to high activity and selectivity over the Ni/BN-a catalysts, which is evidenced by the increased H_2 and CO signal in the MS (Figure S20). The evolution trends of these intermediates in the fourth pulse (CO_2 pulse) are the same as in the second pulse experiments. The results mentioned above clarify the favorable activation of CH_4 and CO_2 over the Ni/BN-a catalysts.

4. CONCLUSIONS

In conclusion, highly active Ni nanocatalysts confined by active edges of boron nitride have been originally developed, and the coking- and sintering-resistant MDR mechanism has also been unraveled. The boundary BO_x species are proved as the active edges over BN to stabilize Ni particles, arising strong sintering

https://doi.org/10.1021/acsami.2c04149
ACS Appl. Mater. Interfaces 2022, 14, 25439−25447

resistance of active Ni, which display an excellent MDR performance and high coking resistance. The etching of BN is suppressed under the buffer of boundary BO_x species. The mutipulse coupling online MS experiments prove that the catalysts with abundant boundary BO_x species can enhance the adsorption and activation of both CH_4 and CO_2. The weak adsorption of CO over the Ni/BN-a catalysts observed by operando DRIFT spectra demonstrates the high selectivity of CO. Moreover, operando DRIFT spectra confirm that the boundary BO_x species are involved in the formation and decomposition of the active bicarbonate (*HCO_3) species. Meanwhile, CH_4 can accelerate the evolution of intermediates, raising the reaction rate. The full decomposition of CH_4 is suppressed and thus the carbon deposition is restricted based on the operando Raman spectrum results. This finding provides a deep insight on edge defects of BN, and a novel approach for the development of coking- and sintering-resistant Ni nanocatalysts for MDR.

■ ASSOCIATED CONTENT

Supporting Information

The Supporting Information is available free of charge at https://pubs.acs.org/doi/10.1021/acsami.2c04149.

Experimental details, performance calculations, additional XRD, TEM, scanning electron microscopy, XPS, CO_2-TPD, CH_4-TPSR, online MS, and in situ Raman results, and discussions (PDF)

■ AUTHOR INFORMATION

Corresponding Author

Dengsong Zhang − *State Key Laboratory of Advanced Special Steel, School of Materials Science and Engineering, International Joint Laboratory of Catalytic Chemistry, Department of Chemistry, College of Sciences, Shanghai University, 200444 Shanghai, China*; orcid.org/0000-0003-4280-0068; Email: dszhang@shu.edu.cn

Authors

Xiaoyu Zhang − *State Key Laboratory of Advanced Special Steel, School of Materials Science and Engineering, International Joint Laboratory of Catalytic Chemistry, Department of Chemistry, College of Sciences, Shanghai University, 200444 Shanghai, China*

Jiang Deng − *State Key Laboratory of Advanced Special Steel, School of Materials Science and Engineering, International Joint Laboratory of Catalytic Chemistry, Department of Chemistry, College of Sciences, Shanghai University, 200444 Shanghai, China*

Tianwei Lan − *State Key Laboratory of Advanced Special Steel, School of Materials Science and Engineering, International Joint Laboratory of Catalytic Chemistry, Department of Chemistry, College of Sciences, Shanghai University, 200444 Shanghai, China*

Yongjie Shen − *State Key Laboratory of Advanced Special Steel, School of Materials Science and Engineering, International Joint Laboratory of Catalytic Chemistry, Department of Chemistry, College of Sciences, Shanghai University, 200444 Shanghai, China*

Wenqiang Qu − *State Key Laboratory of Advanced Special Steel, School of Materials Science and Engineering, International Joint Laboratory of Catalytic Chemistry, Department of Chemistry, College of Sciences, Shanghai University, 200444 Shanghai, China*

Qingdong Zhong − *State Key Laboratory of Advanced Special Steel, School of Materials Science and Engineering, International Joint Laboratory of Catalytic Chemistry, Department of Chemistry, College of Sciences, Shanghai University, 200444 Shanghai, China*

Complete contact information is available at: https://pubs.acs.org/10.1021/acsami.2c04149

Author Contributions

†X.Y.Z. and J.D. contributed equally to this work.

Notes

The authors declare no competing financial interest.

■ ACKNOWLEDGMENTS

This work was financially supported by the National Natural Science Foundation of China (22125604).

■ REFERENCES

(1) Pakhare, D.; Spivey, J. A Review of Dry (CO_2) Reforming of Methane over Noble Metal Catalysts. *Chem. Soc. Rev.* **2014**, *43*, 7813−7837.

(2) Ashcroft, A. T.; Cheetham, A. K.; Green, M. L. H.; Vernon, P. D. F. Partial Oxidation of Methane to Synthesis Gas using Carbon Dioxide. *Nature* **1991**, *352*, 225−226.

(3) Buelens, L. C.; Galvita, V. V.; Poelman, H.; Detavernier, C.; Marin, G. B. Super-Dry Reforming of Methane Intensifies CO_2 Utilization via Le Chatelier's Principle. *Science* **2016**, *354*, 449.

(4) Song, Y.; Ozdemir, E.; Ramesh, S.; Adishev, A.; Subramanian, S.; Harale, A.; Albuali, M.; Fadhel, B. A.; Jamal, A.; Moon, D.; Choi, S. H.; Yavuz, C. T. Dry Reforming of Methane by Stable Ni−Mo Nanocatalysts on Single-Crystalline Mgo. *Science* **2020**, *367*, 777−781.

(5) Xie, K.; Xiao, Y. Active Exsolved Metal-Oxide Interfaces in Porous Single-Crystalline Ceria Monoliths for Efficient and Durable CH_4/CO_2 Reforming. *Angew. Chem., Int. Ed.* **2021**, *61*, No. e202113079.

(6) Jang, W.-J.; Jeong, D.-W.; Shim, J.-O.; Kim, H.-M.; Roh, H.-S.; Son, I. H.; Lee, S. J. Combined Steam and Carbon Dioxide Reforming of Methane and Side Reactions: Thermodynamic Equilibrium Analysis and Experimental Application. *Appl. Energy* **2016**, *173*, 80−91.

(7) He, L.; Li, M.; Li, W.-C.; Xu, W.; Wang, Y.; Wang, Y.-B.; Shen, W.; Lu, A.-H. Robust and Coke-Free Ni Catalyst Stabilized by 1-2 nm-Thick Multielement Oxide for Methane Dry Reforming. *ACS Catal.* **2021**, *11*, 12409−12416.

(8) Yang, B.; Deng, J.; Li, H.; Yan, T.; Zhang, J.; Zhang, D. Coking-Resistant Dry Reforming of Methane over Ni/γ-Al_2O_3 Catalysts by Rationally Steering Metal-Support Interaction. *Iscience* **2021**, *24*, 102747.

(9) Mohammadi, M. M.; Shah, C.; Dhandapani, S. K.; Chen, J.; Abraham, S. R.; Sullivan, W.; Buchner, R. D.; Kyriakidou, E. A.; Lin, H.; Lund, C. R. F.; Swihart, M. T. Single-Step Flame Aerosol Synthesis of Active and Stable Nanocatalysts for the Dry Reforming of Methane. *ACS Appl. Mater. Interfaces* **2021**, *13*, 17618−17628.

(10) Das, S.; Jangam, A.; Jayaprakash, S.; Xi, S.; Hidajat, K.; Tomishige, K.; Kawi, S. Role of Lattice Oxygen in Methane Activation on Ni-Phyllosilicate@$Ce_{1-X}Zr_xO_2$ Core-Shell Catalyst for Methane Dry Reforming: Zr Doping Effect, Mechanism, and Kinetic Study. *Appl. Catal., B* **2021**, *290*, 119998.

(11) Li, K.; Chang, X.; Pei, C.; Li, X.; Chen, S.; Zhang, X.; Assabumrungrat, S.; Zhao, Z.-J.; Zeng, L.; Gong, J. Ordered Mesoporous Ni/La_2O_3 Catalysts with Interfacial Synergism Towards CO_2 Activation in Dry Reforming of Methane. *Appl. Catal., B* **2019**, *259*, 118092.

(12) Managutti, P. B.; Tymen, S.; Liu, X.; Hernandez, O.; Prestipino, C.; Le Gal La Salle, A.; Paul, S.; Jalowiecki-Duhamel, L.; Dorcet, V.; Billard, A.; Briois, P.; Bahout, M. Exsolution of Ni Nanoparticles from A-Site-Deficient Layered Double Perovskites for Dry Reforming of Methane and as An Anode Material dor A Solid Oxide Fuel Cell. *ACS Appl. Mater. Interfaces* **2021**, *13*, 35719−35728.

(13) Sheng, K.; Luan, D.; Jiang, H.; Zeng, F.; Wei, B.; Pang, F.; Ge, J. Ni_xCO_y Nanocatalyst Supported by ZrO_2 Hollow Sphere for Dry Reforming of Methane: Synergetic Catalysis By Ni and Co in Alloy. *ACS Appl. Mater. Interfaces* **2019**, *11*, 24078−24087.

(14) Kim, S. M.; Abdala, P. M.; Margossian, T.; Hosseini, D.; Foppa, L.; Armutlulu, A.; Van Beek, W.; Comas-Vives, A.; Copéret, C.; Müller, C. Cooperativity and Dynamics Increase the Performance of NiFe Dry Reforming Catalysts. *J. Am. Chem. Soc.* **2017**, *139*, 1937−1949.

(15) Tsoukalou, A.; Imtiaz, Q.; Kim, S. M.; Abdala, P. M.; Yoon, S.; Müller, C. R. Dry-Reforming of Methane over Bimetallic Ni−M/La_2O_3 (M=Co, Fe): The Effect of the Rate of $La_2O_2CO_3$ Formation and Phase Stability on the Catalytic Activity and Stability. *J. Catal.* **2016**, *343*, 208−214.

(16) Liang, T.-Y.; Raja, D. S.; Chin, K. C.; Huang, C.-L.; Sethupathi, S. A. P.; Leong, L. K.; Tsai, D.-H.; Lu, S.-Y. Bimetallic Metal−Organic Framework-Derived Hybrid Nanostructures as High-Performance Catalysts for Methane Dry Reforming. *ACS Appl. Mater. Interfaces* **2020**, *12*, 15183−15193.

(17) Jang, W.-J.; Shim, J.-O.; Kim, H.-M.; Yoo, S.-Y.; Roh, H.-S. A Review on Dry Reforming of Methane in Aspect of Catalytic Properties. *Catal. Today* **2019**, *324*, 15−26.

(18) Weng, Q.; Wang, X.; Wang, X.; Bando, Y.; Golberg, D. Functionalized Hexagonal Boron Nitride Nanomaterials: Emerging Properties and Applications. *Chem. Soc. Rev.* **2016**, *45*, 3989−4012.

(19) Liu, Z.; Gong, Y.; Zhou, W.; Ma, L.; Yu, J.; Idrobo, J. C.; Jung, J.; Macdonald, A. H.; Vajtai, R.; Lou, J.; Ajayan, P. M. Ultrathin High-Temperature Oxidation-Resistant Coatings of Hexagonal Boron Nitride. *Nat. Commun.* **2013**, *4*, 2541.

(20) Liu, Y.-R.; Li, X.; Liao, W.-M.; Jia, A.-P.; Wang, Y.-J.; Luo, M.-F.; Lu, J.-Q. Highly Active Pt/BN Catalysts for Propane Combustion: the Roles of Support and Reactant-Induced Evolution of Active Sites. *ACS Catal.* **2019**, *9*, 1472−1481.

(21) Grant, J. T.; Carrero, C. A.; Goeltl, F.; Venegas, J.; Mueller, P.; Burt, S. P.; Specht, S. E.; Mcdermott, W. P.; Chieregato, A.; Hermans, I. Selective Oxidative Dehydrogenation of Propane to Propene using Boron Nitride Catalysts. *Science* **2016**, *354*, 1570.

(22) Zhu, W.; Wu, Z.; Foo, G. S.; Gao, X.; Zhou, M.; Liu, B.; Veith, G. M.; Wu, P.; Browning, K. L.; Lee, H. N.; Li, H.; Dai, S.; Zhu, H. Taming Interfacial Electronic Properties of Platinum Nanoparticles on Vacancy-Abundant Boron Nitride Nanosheets for Enhanced Catalysis. *Nat. Commun.* **2017**, *8*, 15291.

(23) Li, M.; Wang, Y.; Tang, P.; Xie, N.; Zhao, Y.; Liu, X.; Hu, G.; Xie, J.; Zhao, Y.; Tang, J.; Zhang, T.; Ma, D. Graphene With Atomic-Level in-Plane Decoration of h-BN Domains for Efficient Photocatalysis. *Chem. Mater.* **2017**, *29*, 2769−2776.

(24) Lu, W.-D.; Wang, D.; Zhao, Z.; Song, W.; Li, W.-C.; Lu, A.-H. Supported Boron Oxide Catalysts for Selective and Low-Temperature Oxidative Dehydrogenation of Propane. *ACS Catal.* **2019**, *9*, 8263−8270.

(25) Kim, Y.; Kang, S.; Kang, D.; Lee, K. R.; Song, C. K.; Sung, J.; Kim, J. S.; Lee, H.; Park, J.; Yi, J. Single-Phase Formation of Rh_2O_3 Nanoparticles on h-BN Support for Highly Controlled Methane Partial Oxidation to Syngas. *Angew. Chem., Int. Ed.* **2021**, *60*, 25411−25418.

(26) Bu, K.; Kuboon, S.; Deng, J.; Li, H.; Yan, T.; Chen, G.; Shi, L.; Zhang, D. Methane Dry Reforming over Boron Nitride Interface-Confined and LDHs-Derived Ni Catalysts. *Appl. Catal., B* **2019**, *252*, 86−97.

(27) Deng, J.; Bu, K.; Shen, Y.; Zhang, X.; Zhang, J.; Faungnawakij, K.; Zhang, D. Cooperatively Enhanced Coking Resistance via Boron Nitride Coating over Ni-Based Catalysts for Dry Reforming of Methane. *Appl. Catal., B* **2022**, *302*, 120859.

(28) Lu, M.; Zhang, X.; Deng, J.; Kuboon, S.; Faungnawakij, K.; Xiao, S.; Zhang, D. Coking-Resistant Dry Reforming of Methane over BN−Nanoceria Interface-Confined Ni Catalysts. *Catal. Sci. Technol.* **2020**, *10*, 4237−4244.

(29) Wu, J. C. S.; Chou, H.-C. Bimetallic Rh−Ni/BN Catalyst for Methane Reforming with CO_2. *Chem. Eng. J.* **2009**, *148*, 539−545.

(30) Zhang, Z.; Su, J.; Matias, A. S.; Gordon, M.; Liu, Y.-S.; Guo, J.; Song, C.; Dun, C.; Prendergast, D.; Somorjai, G. A.; Urban, J. J. Enhanced and Stabilized Hydrogen Production from Methanol by Ultrasmall Ni Nanoclusters Immobilized on Defect-Rich h-BN Nanosheets. *Proc. Natl. Acad. Sci. U.S.A.* **2020**, *117*, 29442−29452.

(31) Lyalin, A.; Gao, M.; Taketsugu, T. When Inert Becomes Active: A Fascinating Route for Catalyst Design. *Chem. Rec.* **2016**, *16*, 2324−2337.

(32) Dong, J.; Gao, L.; Fu, Q. Hexagonal Boron Nitride Meeting Metal: A New Opportunity and Territory in Heterogeneous Catalysis. *J. Phys. Chem. Lett.* **2021**, *12*, 9608−9619.

(33) Lin, C.; Wu, J. C. S.; Pan, J.-W.; Yeh, C.-T. Characterization of Boron-Nitride-Supported Pt Catalysts for the Deep Oxidation of Benzene. *J. Catal.* **2002**, *210*, 39−45.

(34) Bu, K.; Deng, J.; Zhang, X.; Kuboon, S.; Yan, T.; Li, H.; Shi, L.; Zhang, D. Promotional Effects of B-terminated Defective Edges of Ni/Boron Nitride Catalysts for Coking- and Sintering-Resistant Dry Reforming of Methane. *Appl. Catal., B* **2020**, *267*, 118692.

(35) Cao, Y.; Maitarad, P.; Gao, M.; Taketsugu, T.; Li, H.; Yan, T.; Shi, L.; Zhang, D. Defect-Induced Efficient Dry Reforming of Methane over Two-Dimensional Ni/h-Boron Nitride Nanosheet Catalysts. *Appl. Catal., B* **2018**, *238*, 51−60.

(36) Dong, J.; Fu, Q.; Li, H.; Xiao, J.; Yang, B.; Zhang, B.; Bai, Y.; Song, T.; Zhang, R.; Gao, L.; Cai, J.; Zhang, H.; Liu, Z.; Bao, X. Reaction-Induced Strong Metal−Support Interactions between Metals and Inert Boron Nitride Nanosheets. *J. Am. Chem. Soc.* **2020**, *142*, 17167−17174.

(37) Qu, W.; Wang, P.; Gao, M.; Hasegawa, J.-Y.; Shen, Z.; Wang, Q.; Li, R.; Zhang, D. Delocalization Effect Promoted the Indoor Air Purification via Directly Unlocking the Ring-Opening Pathway of Toluene. *Environ. Sci. Technol.* **2020**, *54*, 9693−9701.

(38) Huang, C.; Chen, C.; Zhang, M.; Lin, L.; Ye, X.; Lin, S.; Antonietti, M.; Wang, X. Carbon-Doped BN Nanosheets for Metal-Free Photoredox Catalysis. *Nat. Commun.* **2015**, *6*, 7698.

(39) Goodman, E. D.; Schwalbe, J. A.; Cargnello, M. Mechanistic Understanding and the Rational Design of Sinter-Resistant Heterogeneous Catalysts. *ACS Catal.* **2017**, *7*, 7156−7173.

(40) Song, T.; Dong, J.; Li, R.; Xu, X.; Hiroaki, M.; Yang, B.; Zhang, R.; Bai, Y.; Xin, H.; Lin, L.; Mu, R.; Fu, Q.; Bao, X. Oxidative Strong Metal−Support Interactions between Metals and Inert Boron Nitride. *J. Phys. Chem. Lett.* **2021**, *12*, 4187−4194.

(41) Wang, T.-C.; Yin, J.-L.; Guo, X.-J.; Chen, Y.; Lang, W.-Z.; Guo, Y.-J. Modulating the Crystallinity of Boron Nitride for Propane Oxidative Dehydrogenation. *J. Catal.* **2021**, *393*, 149−158.

(42) Zhou, Y.; Lin, J.; Li, L.; Pan, X.; Sun, X.; Wang, X. Enhanced Performance of Boron Nitride Catalysts with Induction Period for the Oxidative Dehydrogenation of Ethane to Ethylene. *J. Catal.* **2018**, *365*, 14−23.

(43) Zhang, X.; Deng, J.; Pupucevski, M.; Impeng, S.; Yang, B.; Chen, G.; Kuboon, S.; Zhong, Q.; Faungnawakij, K.; Zheng, L.; Wu, G.; Zhang, D. High-Performance Binary Mo−Ni Catalysts for Efficient Carbon Removal during Carbon Dioxide Reforming of Methane. *ACS Catal.* **2021**, *11*, 12087−12095.

(44) Ferrari, A. C.; Robertson, J. Interpretation of Raman Spectra of Disordered and Amorphous Carbon. *Phys. Rev. B: Condens. Matter Mater. Phys.* **2000**, *61*, 14095−14107.

(45) Wu, J.; Han, W.-Q.; Walukiewicz, W.; Ager, J. W.; Shan, W.; Haller, E. E.; Zettl, A. Raman Spectroscopy and Time-Resolved Photoluminescence of BN and $B_xC_yN_z$ Nanotubes. *Nano Lett.* **2004**, *4*, 647−650.

(46) Reich, S.; Ferrari, A. C.; Arenal, R.; Loiseau, A.; Bello, I.; Robertson, J. Resonant Raman Scattering in Cubic and Hexagonal

Boron Nitride. *Phys. Rev. B: Condens. Matter Mater. Phys.* **2005**, *71*, 205201.
(47) Sainsbury, T.; Satti, A.; May, P.; Wang, Z.; Mcgovern, I.; Gun'ko, Y. K.; Coleman, J. Oxygen Radical Functionalization of Boron Nitride Nanosheets. *J. Am. Chem. Soc.* **2012**, *134*, 18758−18771.
(48) Zhang, S.; Tang, L.; Yu, J.; Zhan, W.; Wang, L.; Guo, Y.; Guo, Y. Spherical Ni Nanoparticles Supported by Nanosheet-Assembled Al_2O_3 for Dry Reforming of CH_4: Elucidating the Induction Period and Its Excellent Resistance to Coking. *ACS Appl. Mater. Interfaces* **2021**, *13*, 58605−58618.
(49) Wang, Y.; Yao, L.; Wang, Y.; Wang, S.; Zhao, Q.; Mao, D.; Hu, C. Low-Temperature Catalytic CO_2 Dry Reforming of Methane on Ni-Si/ZrO_2 Catalyst. *ACS Catal.* **2018**, *8*, 6495−6506.
(50) Németh, M.; Schay, Z.; Srankó, D.; Károlyi, J.; Sáfrán, G.; Sajó, I.; Horváth, A. Impregnated Ni/ZrO_2 and Pt/ZrO_2 Catalysts in Dry Reforming of Methane: Activity Tests in Excess Methane and Mechanistic Studies with Labeled $^{13}CO_2$. *Appl. Catal., A* **2015**, *504*, 608−620.
(51) Das, S.; Ashok, J.; Bian, Z.; Dewangan, N.; Wai, M. H.; Du, Y.; Borgna, A.; Hidajat, K.; Kawi, S. Silica−Ceria Sandwiched Ni Core−Shell Catalyst for Low Temperature Dry Reforming of Biogas: Coke Resistance and Mechanistic Insights. *Appl. Catal., B* **2018**, *230*, 220−236.
(52) Cárdenas-Arenas, A.; Quindimil, A.; Davó-Quiñonero, A.; Bailón-García, E.; Lozano-Castelló, D.; De-La-Torre, U.; Pereda-Ayo, B.; González-Marcos, J. A.; González-Velasco, J. R.; Bueno-López, A. Isotopic and in situ DRIFTS Study of the CO_2 Methanation Mechanism using Ni/CeO_2 and Ni/Al_2O_3 Catalysts. *Appl. Catal., B* **2020**, *265*, 118538.
(53) Li, H.; Tian, H.; Chen, S.; Sun, Z.; Liu, T.; Liu, R.; Assabumrungrat, S.; Saupsor, J.; Mu, R.; Pei, C.; Gong, J. Sorption Enhanced Steam Reforming of Methanol for High-Purity Hydrogen Production over Cu-Mgo/Al_2O_3 Bifunctional Catalysts. *Appl. Catal., B* **2020**, *276*, 119052.
(54) Huynh, H. L.; Zhu, J.; Zhang, G.; Shen, Y.; Tucho, W. M.; Ding, Y.; Yu, Z. Promoting Effect of Fe on Supported Ni Catalysts in CO_2 Methanation by in situ DRIFTS and DFT Study. *J. Catal.* **2020**, *392*, 266−277.
(55) Ni, J.; Chen, L.; Lin, J.; Kawi, S. Carbon Deposition on Borated Alumina Supported Nano-Sized Ni Catalysts for Dry Reforming of CH_4. *Nano Energy* **2012**, *1*, 674−686.

Recommended by ACS

Unraveling the Unique Promotion Effects of a Triple Interface in Ni Catalysts for Methane Dry Reforming

Xiaoyu Zhang, Dengsong Zhang, *et al.*

MARCH 11, 2023
INDUSTRIAL & ENGINEERING CHEMISTRY RESEARCH

READ

Promoting Methane Dry Reforming over Ni Catalysts via Modulating Surface Electronic Structures of BN Supports by Doping Carbon

Xiaoyu Zhang, Dengsong Zhang, *et al.*

NOVEMBER 04, 2022
ACS CATALYSIS

READ

Constructing Efficient Nickel Catalysts on CeO_x Nanoparticles Stabilized Using γ-Al_2O_3 to Catalyze Ammonia Decomposition for Hydrogen Production

Lu-Lu Zhou, Chun-Jiang Jia, *et al.*

FEBRUARY 02, 2023
ACS APPLIED NANO MATERIALS

READ

Atomically Incorporating Ni into Mesoporous CeO_2 Matrix via Synchronous Spray-Pyrolysis as Efficient Noble-Metal-Free Catalyst for Low-Temperature CO Oxidation

Na Sun, Long Kuai, *et al.*

DECEMBER 30, 2022
INORGANIC CHEMISTRY

READ

Get More Suggestions >

https://doi.org/10.1021/acsami.2c04149
ACS Appl. Mater. Interfaces 2022, 14, 25439−25447